APPLIED PHYSICS

Beating thermal noise in a dynamic signal measurement by a nanofabricated cavity optomechanical sensor

Mingkang Wang[1,2], Diego J. Perez-Morelo[1,2], Georg Ramer[2,3,4], Georges Pavlidis[3], Jeffrey J. Schwartz[2,3], Liya Yu[5], Robert Ilic[5], Andrea Centrone[3], Vladimir A. Aksyuk[1]*

Copyright © 2023 The Authors, some rights reserved; exclusive licensee American Association for the Advancement of Science. No claim to original U.S. Government Works. Distributed under a Creative Commons Attribution NonCommercial License 4.0 (CC BY-NC).

Thermal fluctuations often impose both fundamental and practical measurement limits on high-performance sensors, motivating the development of techniques that bypass the limitations imposed by thermal noise outside cryogenic environments. Here, we theoretically propose and experimentally demonstrate a measurement method that reduces the effective transducer temperature and improves the measurement precision of a dynamic impulse response signal. Thermal noise–limited, integrated cavity optomechanical atomic force microscopy probes are used in a photothermal-induced resonance measurement to demonstrate an effective temperature reduction by a factor of ≈25, i.e., from room temperature down as low as ≈12 K, without cryogens. The method improves the experimental measurement precision and throughput by >2×, approaching the theoretical limit of ≈3.5× improvement for our experimental conditions. The general applicability of this method to dynamic measurements leveraging thermal noise–limited harmonic transducers will have a broad impact across a variety of measurement platforms and scientific fields.

INTRODUCTION

The rapid development of nanomechanics in synergy with technological advances in acoustics, optics, and electronics has spurred several successful sensing architectures, including nanoelectromechanical systems, atomic force microscopy (AFM), and cavity optomechanical sensors. The unprecedented sensing ability and ultralow instrumental detection noise levels of these systems have led to numerous achievements, such as measurement of Brownian vibrations at cryogenic temperatures (*1*), detection of single spins (*2*), single-molecule mass spectrometry (*3*), and ultrasensitive measurements of other physical quantities (*4*–*9*). Specifically, the recent development of cavity optomechanical sensors based on low-noise laser sources and high-quality photonic cavities has enabled measurement of quantum zero-point fluctuations in mechanical resonators, reaching the standard quantum limit (*10*) at ultracold (millikelvin) temperatures. However, at room temperature, the precision of force measurements is typically limited by the Langevin force, while the position measurements are limited by the associated Brownian motion, i.e., the mechanical thermal noise (*11*). Thermal noise also remains the limiting factor, even in cryogenic temperatures, for ultrasensitive carbon nanotube resonators (*1*).

Analogous to the charge carriers' thermal agitation for Johnson-Nyquist noise in the electrical domain, the mechanical thermal noise is induced by the excitation of the sensor's mechanical parts by the Langevin force. The mechanical thermal noise spectral density typically has a Lorentzian shape, given by the mechanical responsivity, and obeys the equipartition theorem, i.e., the integrated noise power equals $k_bT/2$, for each degree of freedom, where k_b is the Boltzmann constant and T is the temperature. At room temperature, the thermal noise power in nanomechanical resonators with low mass and stiffness is often well above the instrumental detection noise floor over a broad range of frequencies near the resonator eigenfrequencies. Since high-precision sensors typically operate on or near resonance for increased gain, thermal noise limits their sensitivities. Because of its ubiquity, thermal noise is widely used for calibration (*12*–*14*) and measurement (*15*–*17*) of nanomechanical sensors. For example, in conventional AFM setups, thermal noise is typically well above detection noise at frequencies near the AFM cantilever resonances and it is used to obtain the probe's mechanical properties. However, thermal noise also poses a detection limit, which hinders the sensitivity potential of advanced sensors [e.g., AFM (*18*, *19*) and microelectromechanical systems (*20*–*22*)] at room temperature.

Many strategies have been used to overcome the thermal noise limit and to reduce thermal fluctuations in nanomechanical resonators (*23*), including sideband cooling of optomechanical systems (*24*), feedback-controlled stochastic cooling (*25*), and elastic strain. In practice, however, none of these methods can be easily or broadly implemented across sensing platforms because they require complicated setups and have suffered from poor long-term stability. Averaging the signal from repeatable events, such as continuous measurements of stable states or repeated measurement of the same transient events, is a simple and commonly used strategy to reduce thermal noise and uncorrelated detection noise. However, long-time averaging is not possible for nonrepeatable stochastic processes or for systems with a fast drift. Furthermore, long averaging times and associated low-measurement throughputs are also major obstacles for scanning probe imaging, such as AFM and scanning tunneling microscopy. Therefore, new methods for

[1]Microsystems and Nanotechnology Division, National Institute of Standards and Technology, Gaithersburg, MD 20899, USA. [2]Institute for Research in Electronics and Applied Physics, University of Maryland, College Park, MD 20742, USA. [3]Nanoscale Devices Characterization Division, National Institute of Standards and Technology, Gaithersburg, MD 20899, USA. [4]Institute of Chemical Technologies and Analytics, TU Wien, Getreidemarkt 9, 1060 Vienna, Austria. [5]Center for Nanoscale Science and Technology, National Institute of Standards and Technology, Gaithersburg, MD 20899, USA.
*Corresponding author. Email: vladimir.aksyuk@nist.gov

Downloaded from https://www.science.org on March 15, 2023

overcoming the thermal noise limit are strongly desirable in many widespread sensing applications.

The present work aims to beat the thermal noise limit and, more broadly, to advance nanomechanical sensing by increasing its throughput and precision. First, we derive a thermal fluctuation estimator that determines, with the lowest possible uncertainty, the thermal fluctuations (noise) for mechanical resonators at steady states in the presence of large detection noise. This optimally estimated thermal motion is extrapolated forward in time taking advantage of the intrinsic time-correlated nature of thermal position fluctuations within the dissipation time scale. Thereby, we can distinguish and remove the extrapolated thermal noise from a dynamic measurement signal of interest, effectively reducing the temperature of the sensor and, therefore, suppressing the signal uncertainty contributed by thermal noise. We experimentally validate this thermal noise subtraction method by leveraging thermal noise–limited cavity optomechanical AFM probes as a testing platform. To demonstrate its reliability in a practical dynamic signal measurement, we apply the above strategy for nanoscale infrared (IR) spectroscopy experiments based on the photothermal-induced resonance (PTIR) technique (*26*–*28*), in which an impulsive excitation and subsequent ringdown are measured. Application of this thermal noise subtraction method decreases the uncertainty of the PTIR signal by ≈2×, leading to a twofold increase in either measurement precision or throughput. For the experimental conditions used here, we identify a ≈3.5× theoretical improvement limit of the thermal fluctuation uncertainty, with the smaller experimental improvement attributed to nonthermal factors such as the laser jitter. In contrast to previous attempts that overcome the thermal noise limit (*23*–*25*), our method is broadly applicable to commonly used micro- and nanomechanical sensors and improves the measurement precision for both single-shot and repeatable dynamic signals with deterministic temporal profiles. Beyond nanomechanical sensors, the general applicability of the thermal noise estimation and subtraction strategy can affect a broad class of measurements that use harmonic resonator transducers (e.g., optical, acoustic, and radiofrequency) limited by thermal noise.

RESULTS

Thermal noise–limited high-precision measurements

Precision measurements often use resonators with high-quality factors to provide high gain near their eigenfrequencies. At room temperature, these resonance-based measurements are limited by the stochastic Langevin force–induced thermal motion that is also amplified around the resonance. One typical indicator of this condition is given by the noise power spectral density (Fig. 1A) where the thermal noise spectrum (purple) is well above the white detection noise floor (blue) for a range of frequencies several times wider than its dissipation rate Γ. In our previous work (*17*), we demonstrated how the thermal noise can be used for rapid, dynamic frequency estimation in the presence of strong detection noise. The analysis therein provides the firm theoretical ground for considering the effects of thermal noise and detection noise for measurements at the steady states. These two types of stochastic noise are intrinsically different, since the thermal noise has an autocorrelation time scale ≈ 1/Γ, while the detection noise is uncorrelated, allowing for discrimination between them at steady states (Fig. 1A). The thermal fluctuations, accurately estimated in the steady-state, can be extrapolated with low uncertainty to the subsequent transient state. By removing the estimated thermal noise in the transient state, the signal-to-noise ratio is improved, especially in the subsequent ≈1/Γ time scale where the estimation has high precision. If the desired transient signal is within the 1/Γ time scale, this thermal noise subtraction procedure will largely improve the measurement precision, e.g., the signal of PTIR used for chemical imaging occurs shortly after the impulsive excitation (*27*, *28*).

Following from the fluctuation dissipation theorem, the thermal force noise decreases with lower values of damping Γ; therefore, high-precision measurements typically use resonators with long autocorrelation time scale 1/Γ, exceeding the duration of many transient signals of interest. This presents a general opportunity to improve measurement precision of transient signals by removing the thermal mechanical noise.

Transient measurements not only are common in fundamental research but also have wide practical applications. One example is the PTIR technique (*26*–*28*), an AFM-based IR nanospectroscopy method. In these measurements, an AFM probe is used to transduce the transient thermal expansion of a sample due to absorption of short mid-IR laser pulses. In place of conventional AFM probe, in this work, we use ultrasensitive optomechanical probes (*29*). Figure 1C depicts the equivalent mechanical model of this measurement. At steady state, the AFM probe with fundamental eigenfrequency ω_0 and effective mass m is at thermal equilibrium at ambient temperature T and subject to the Langevin force and dissipation Γ according to the fluctuation-dissipation theorem. At $t = t_0$, a short laser pulse (≈10 ns) rapidly offsets the "contact point" by B due to the fast photothermal expansion of the sample. During the transient state after the pulse, the pulse puts the probe into oscillation while the contact point returns to the original position according to the thermal relaxation process of the sample surface with a thermal constant τ (*29*, *30*). As result, the signal of this measurement can be separated in time by $t = t_0$ into two stages, as shown in the lower panel of Fig. 1C. At $t < t_0$ (yellow area), the readout is just a linear combination of thermal noise and detection noise. At $t > t_0$, the dynamics of the probe, in addition to the noise, can be modeled as (*29*, *30*)

$$S = S_{\mathrm{osc}} + S_{\mathrm{exp}} \tag{1}$$

where $S_{\mathrm{osc}} = A\cos(\omega_0 t + \phi)e^{-\Gamma t/2}$ and $S_{\mathrm{exp}} = Be^{-t/\tau}$ are the ringdown term of the probe and the thermal relaxation term of the sample. These two terms from the AFM probe operating as a linear mechanical resonator are independent of each other. We note that while the PTIR signal obtained with the optomechanical resonator AFM probes (*30*) used here contains both S_{osc} and S_{exp}, the signal obtained with conventional AFM probes (*31*) contains only the S_{osc} term, due to the much smaller measurement bandwidth. Here, we define the time of the laser pulse $t_0 = 0$. A and B are the initial mode amplitude and the initial deformation of the sample after the pulse. The transient quantities of interest in this measurement are A and B.

By leveraging narrow-line, wavelength tunable lasers, PTIR provides rich information on the sample nanoscale composition and thermal properties. For example, measuring S_{osc} as a function of the mid-IR excitation wavelength yields nanoscale IR spectra that enable the identification of chemical groups (*32*), materials (*33*, *34*), secondary structure, (*35*) bandgap (*36*), and the characterization of optical modes such as plasmons (*37*) and polaritons (*38*).

Downloaded from https://www.science.org on March 15, 2023

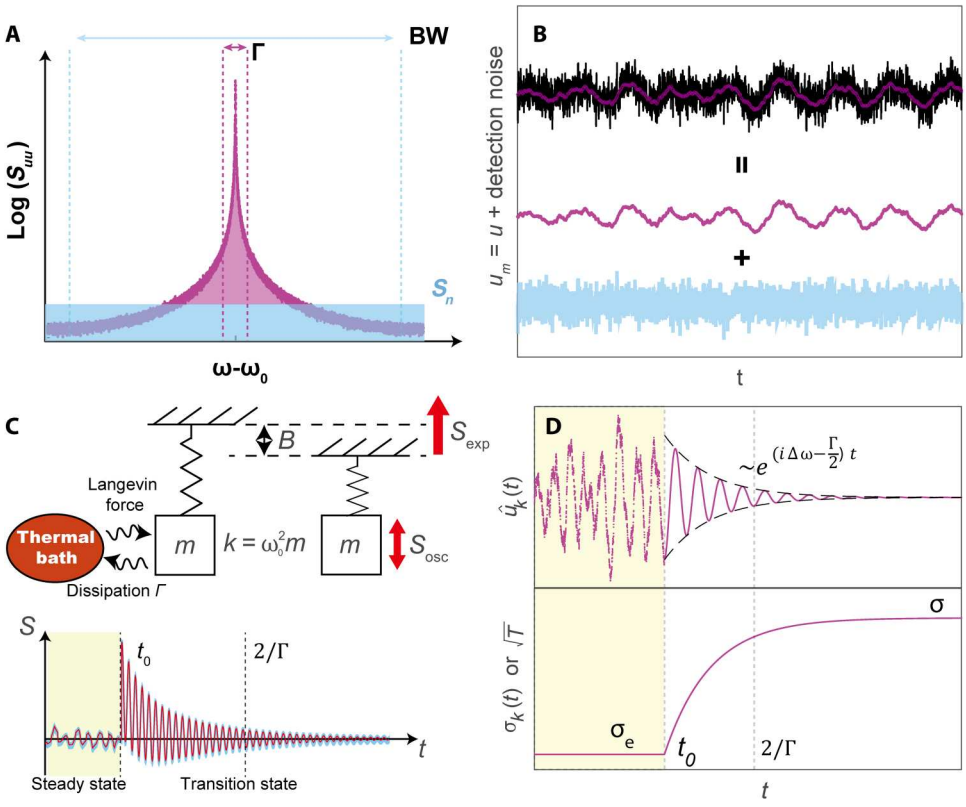

Fig. 1. Distinguishing thermal fluctuations from instrumental detection noise. (**A**) Power spectral density of a harmonic oscillator at thermal equilibrium. The purple and blue areas correspond to the thermal fluctuations and the detection noise spectra, respectively. The purple and blue dashed lines delimit the damping and detection bandwidths. (**B**) Numerically modeled displacement measurements u_m (black) consisting of correlated thermal fluctuations u (purple) and uncorrelated detection noise (blue). (**C**) Schematic of a harmonic oscillator at steady-state thermal equilibrium and after a transient perturbation, which offsets the contact point by B. Bottom: Schematic of the measured position of the oscillator relative to the contact point. The yellow and white area corresponds to the steady-state and the transient impulse response before and after the perturbation at t_0, respectively. The majority of the transient signal occurs within the thermal noise autocorrelation time period, $t < 2/\Gamma$. (**D**) Estimations of $\hat{u}_k(t)$ and $\sigma_k(t)$ in the steady-state range (yellow background) and in the transient response range (white background) are obtained by Eqs. 2 and 3 and Eqs. 4 and 5, respectively. The uncertainty is low within the thermal noise correlation time frame, $t < 2/\Gamma$.

In addition, the high bandwidth and fast time resolution afforded by the nanophotonic AFM probes used here enable measuring the time-domain sample relaxation, S_{exp}, which can provide the thermal conductivity (*29*, *30*) of the sample and its interfacial thermal conductance with the substrate with nanoscale resolution (*30*). However, as with other high-precision sensors based on resonance, the AFM sensitivity is ultimately limited by thermal noise. Furthermore, long-time averaging to reduce thermal noise is undesirable in AFM due to the low measurement throughput and the associated lateral drift of the AFM scanner. A method to distinguish and remove the thermal noise from the AFM transient signal is generally needed to improve the measurement precision and increase the throughput.

Here, we consider a fast transient offset of the contact point by B at $t = t_0$. However, we emphasize that this method applies to any transition under transient perturbations (duration $\ll 1/\Gamma$) such as delta functions or step functions (whose time derivative is a delta function) for the energy, position, velocity, force, etc.

Thermal fluctuation estimation in the presence of detection noise

To beat the thermal noise limit, it is critical to distinguish the thermal noise from the detection noise background and other dynamic signals as shown in Fig. 1B. This is not trivial for highly dynamic signal measurements whose detection bandwidth BW $\gg \Gamma$, as we discuss below.

We consider a simple but general case—a harmonic oscillator with coordinate x at thermal equilibrium. Without loss of generality, we convert the fast motion into a rotating frame of frequency ω and define a slow variable u via $x = \frac{1}{2}(ue^{i\omega t} + u^* e^{-i\omega t})$. The oscillator of eigenfrequency ω_0 and dissipation rate Γ is subject to zero-mean Gaussian Langevin force, inducing mechanical fluctuations with variance $\langle |u|^2 \rangle = 2\sigma^2$, detected with zero-mean Gaussian detection noise with variance $\langle |u_m - u|^2 \rangle = 2\sigma_n^2$, where u is the actual displacement due to the Langevin force and u_m is the measured displacement including detection noise in the rotating frame. $x_m = \frac{1}{2}(u_m e^{i\omega t} + u_m{}^* e^{-i\omega t})$ is the measured signal in the time domain, corresponding to S in Eq. 1. Defined by the equipartition theorem, the area of thermal noise spectrum (purple area in Fig. 1A) is equal to $\sigma^2 = \frac{k_b T}{m\omega_0{}^2}$ where k_b is the Boltzmann constant. Distinct

Downloaded from https://www.science.org on March 15, 2023

from σ^2 (which is a constant at constant T), σ_n^2 linearly increases with bandwidth $\propto BW \times S_n$, where S_n is the detection noise spectral density (blue area in Fig. 1A). For large bandwidth measurements, which are necessary for measuring dynamics signals, the spectrally integrated detection uncertainty σ_n^2 can be comparable or even larger than the thermal uncertainty σ^2.

At this steady equilibrium state, we estimate (distinguish) the thermal fluctuations $U_k = \{u_1, \ldots u_k\}$ from measured data $U_{m,k} = \{u_{m,1}, \ldots u_{m,k}\}$ containing strong instrumental detection noise using a Bayesian estimation method, i.e., the estimated result (prior knowledge) is updated once a new measurement point is obtained. We define $\hat{u}_k$ as the estimated position immediately after the first k-measured data points and σ_k^2 as its uncertainty (*17*)

$$\frac{1}{\sigma_k^2} = \frac{1}{\sigma_{k-1}^2 e^{-\Gamma dt} + \sigma_{dt}^2} + \frac{1}{\sigma_n^2} \tag{2}$$

$$\hat{u}_k = \left[\frac{1}{\sigma_{k-1}^2 e^{-\Gamma dt} + \sigma_{dt}^2} e^{\left(i\Delta\omega - \frac{\Gamma}{2}\right)dt}\hat{u}_{k-1} + \frac{1}{\sigma_n^2}u_{m,k}\right] \times \left(\frac{1}{\sigma_{k-1}^2 e^{-\Gamma dt} + \sigma_{dt}^2} + \frac{1}{\sigma_n^2}\right)^{-1} \tag{3}$$

where dt is the time interval between data points, $\Delta\omega = \omega - \omega_0$ is the frequency detuning in the rotating frame, and $\sigma_{dt}^2 = \Gamma dt\sigma^2$ is the variance of thermal diffusion within dt. The detailed derivation can be found in (*17*), but the simple conclusion is that, by inputting the continuously measured position $U_{m,k} = \{u_{m,1}, \ldots u_{m,k}\}$ to Eq. 3, we obtain the optimally estimated thermal noise trajectory $\hat{U}_k = \{\hat{u}_1, \ldots \hat{u}_k\}$ with the theoretically lowest possible uncertainty σ_k (Eq. 2). When the detection noise is low, after a large number of measurements k, σ_k converge to $\sigma_e = \frac{\sqrt{\eta^2+4}-\eta}{2}\eta\sigma^2 \ll \sigma$, where the detection noise ratio $\eta = \sqrt{\frac{\sigma_n^2 \Gamma dt}{\sigma^2}} \ll 1$ for high-precision sensors (*17*). In such a case, if we subtract the estimated thermal noise from the measurement record, the resulting signal $U_{m,k} - \hat{U}_k$ would be as if the measurement was done on an equivalent sensor physically cooled down to an effective temperature $T_{\text{eff}} = \frac{\sigma_e^2}{\sigma^2} T \ll T$.

Next, we extend the estimation from steady states to transient responses. The thermal mechanical motion is strongly correlated within the ringdown time interval $1/\Gamma$. This means that, based only on position measurements at $t < 0$, one can predict the position at $0 \le t < 1/\Gamma$ with high confidence. By removing the term associated with new data points in Eqs. 2 and 3, we get (see Materials and Methods)

$$\sigma_k^2(t) = \sigma^2 + [\sigma_k^2(0) - \sigma^2]e^{-\Gamma t} \tag{4}$$

$$\hat{u}_k(t) = \hat{u}_k(0)e^{\left(i\Delta\omega - \frac{\Gamma}{2}\right)t} \tag{5}$$

where uncertainty $\sigma_k^2(t)$ increases from $\sigma_k^2(0) = \sigma_e^2$ at $t = 0$ and approaches σ^2 asymptotically at $t \gg 1/\Gamma$ due to thermal diffusion, while the most likely position $\hat{u}_k(t)$ decays exponentially from the initial thermal state $\hat{u}_k(0) = \hat{u}_{k-1}$ to 0. As the elapsed time from the last measurement increases, the uncertainty of the extrapolation grows, equivalent to the temperature increasing from the "cooled steady state," thermalizing with the thermal bath. However, the thermalization time scale and the transient impulse response time scale are both $\approx 2/\Gamma$ (Fig. 1, C and D). Thus, the useful part of the signal, during the transition, is mostly encompassing the time period over which the sensor effectively cooled to a lower temperature (i.e., with low thermal noise uncertainty) and high precision.

The estimation of thermal noise from steady states to transient states is shown in Fig. 1D. Before t_0, $\sigma_k(t) \propto \sqrt{T_{\text{eff}}}$ is at its steady-state value of $\sigma_e^2 \ll \sigma^2$ based on Eq. 2. The system is "cold," and the thermal noise is low. After t_0, during the transient response, no new information (i.e., no new data points) is provided and $\sigma_k(t)$, given by Eq. 4, increases converging to the original thermal uncertainty σ after thermalization time $\approx 2/\Gamma$ as the correlation decreases with time. In summary, we estimate the thermal fluctuations at steady states before the onset of dynamic signals using Eqs. 2 and 3 and extend the estimation to the time range over which most of the dynamic signal occurs using Eqs. 4 and 5. This method not only gives good estimates but also provides well-defined uncertainties, a crucial aspect for analyzing dynamic signals in practical applications, e.g., for PTIR.

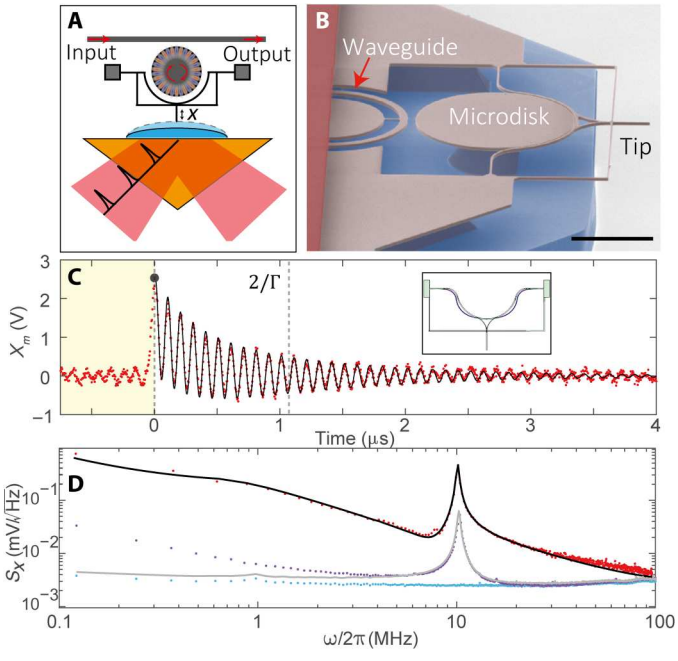

Fig. 2. PTIR measurement. (**A**) Schematic of PTIR measurement setup. The sample (blue area) on top of a ZnSe prism absorbs energy from the pulsed laser, thermally expands, and excites the nanophotonic AFM probe. The mechanical motion of the probe is measured optomechanically by an on-chip optical microdisk. (**B**) False-colored scanning electron micrograph of a nanophotonic AFM probe. Scale bar, 5 μm. (**C**) Time domain tip displacement (x_m, red dots) before and after a laser pulse excitation around $t = 0$ μs. The yellow area marks times in which the resonator is in thermal equilibrium. The second dashed line labels $t = \frac{2}{\Gamma} = 1.09$ μs. The black trace is the fit S based on Eq. 1. Inset: Fundamental in-plane mode shape. (**D**) Magnitude of the Fourier transform of the signal at equilibrium [purple dots, corresponding to the yellow area in (C)] and during the ringdown [red dots, corresponding to the no-color area in (C)]. The gray line is the Lorentzian fit to the purple dots summed with the detection noise floor (blue dots). The detection noise floor is taken when the transduction gain of the AFM probe is set to nearly zero. The black line is the magnitude of the Fourier transform of fit to Eq. 5 in (C).

Downloaded from https://www.science.org on March 15, 2023

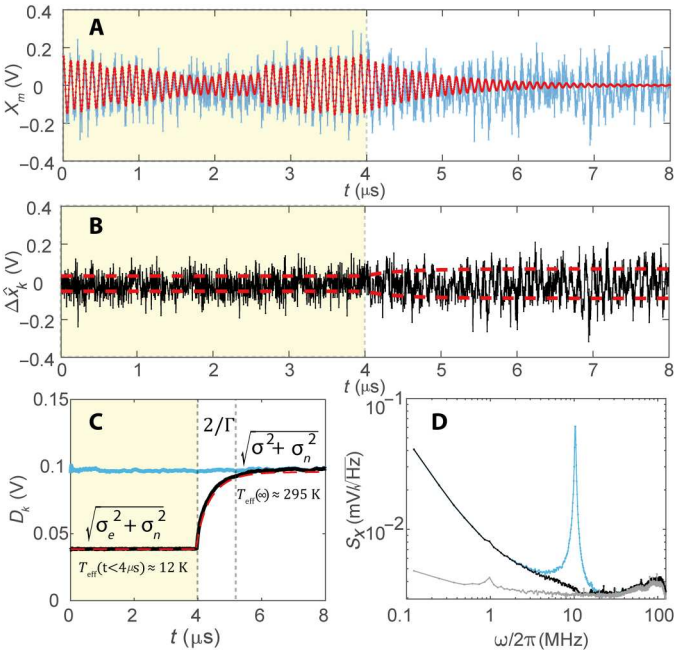

Fig. 3. Thermal noise estimation for the nanophotonic AFM probe. (**A**) Measured (estimated) thermal fluctuations are shown as blue (red) dots. At $t < 4$ μs, the estimation is iterated using Eqs. 2 and 3. At $t > 4$ μs, the estimation continues based on the prior measured data at $t < 4$ μs using Eq. 5. (**B**) The residual of the signal after removing the estimated thermal fluctuations is shown as black dots. The red dashed lines show its one SD uncertainty. (**C**) SD of the residual before (after) removing the estimated thermal fluctuations is shown as blue (black) dots, estimated from 1000 independent measurements. The red dashed line shows the theoretical prediction given by Eqs. 2 and 4 before and after $t = 4$ μs, respectively. (**D**) Magnitude of the Fourier transform of the signal at $t < 4$ μs before (after) removing estimated thermal fluctuations is shown as blue (black) dots. The gray line shows the detection noise floor measured separately.

PTIR setup

In this work, we use a custom PTIR setup (*31*), equipped with a cavity optomechanical AFM probe detection platform (*29*), as a test bed for the effective cooling method, i.e., thermal noise estimation and subtraction process. The PTIR technique is a typical transient impulse response measurement whose signals are mostly within the correlated period (< 2/Γ). Besides the low detection noise, the optomechanical transduction scheme (*29*) guarantees that its thermal noise power spectrum is well above the detection noise floor in a broad range of frequencies at room temperature. These two factors make this platform a good test bed for overcoming the thermal noise limit in dynamic signals. The effective cooling method can be applied to the PTIR data offline, including to boxcar averaged data, and therefore, it does not require any fast in situ data processing.

The nanophotonic PTIR setup (Fig. 2A) uses a nanophotonic AFM probe shown in Fig. 2B. A silicon microdisk of 10 μm diameter, supporting optical whispering gallery modes (WGMs), is evanescently coupled to a mechanical cantilever across a ≈200-nm gap. The mechanical resonator was engineered to include a sharp tip and a supporting frame to increase the stiffness of the fundamental in-plane mode (hereafter mechanical mode), with the goal of suppressing its thermal fluctuations and increasing its bandwidth (*30*). The tip (≈30-nm radius) is operated in contact with the sample (contact mode; Fig. 1A) and is characterized by a mechanical in-contact lowest eigenfrequency of ≈10 MHz, which is advantageous for imaging with high spatial resolution (*39*). The rapid thermal expansion of the sample excites efficiently only the fundamental in-plane mode (Fig. 2C, inset) of the cantilever since the mode shape and symmetry couple to the excitation well. The probe's mechanical excitation modulates the frequency of WGMs in the microdisk via optomechanical coupling. Excitation and detection of the WGMs are implemented by an on-chip waveguide. When the 1550-nm continuous wave detection laser is tuned on the shoulder of the WGM resonance, the detected light intensity measured by a photodetector is proportional to the mechanical response of the probe.

As shown in Fig. 2A, in PTIR, a series of laser pulses (10 ns long, repetition rate of 100 kHz) are incident on a sample from the bottom in a total internal reflection configuration. With the absorption of a light pulse, the sample heats up and expands on the same short time scale, as illustrated in Fig. 1C, where the contact point is at the sample surface. The nanophotonic AFM probe in contact with the sample is excited into oscillation by the rapid thermal expansion, with amplitude proportional to the wavelength-dependent absorption coefficient of the sample (*29*, *40*).

Figure 2C shows the probe excitation obtained when illuminating a 200-nm-thick SU-8 (please see the "Commercial products disclaimer" section in Materials and Methods) polymer sample at 2920 cm^{-1}. The 5-μs-long signal recorded with a sampling time interval $dt = 4$ ns can be separated into two stages. Like the schematic in Fig. 1C, in the first stage ($t < 0$), the probe in contact with the sample is in thermal equilibrium. It shows thermal fluctuations with thermal noise spectral density presented as the purple dots in Fig. 2D. Its Lorentzian fit and a separately measured detection noise floor (blue dots) are shown as a gray line with eigenfrequency $\omega_0/2\pi \approx 10.26$ MHz and damping coefficient $\Gamma/2\pi \approx 0.29$ MHz. The deviation at low frequencies is from the slow distance drift between the probe and the sample holders. The thermal noise is well above the detection noise floor in a broad range of frequencies (≈10 MHz around its eigenfrequency). At the end of the first stage, a 10-ns-long laser pulse heats the sample, kicking the probe instantly (10 ns $\ll 1/\Gamma$) to the position of maximum displacement (black dot in Fig. 2C). In the second stage ($t > 0$), the mechanical mode excitation exponential decays (ringdown) as described by Eq. 1. During ringdown, the timeframe of the thermal noise estimation with low uncertainty (Fig. 1D, bottom) and the signal with large magnitude (Fig. 2C) inherently overlap at $0 < t \lesssim 2/\Gamma$. Therefore, thermal subtraction is effective in increasing the precision of the dynamic signal. The black line in Fig. 2C shows the fitting result for S using Eq. 1, where $\Gamma h 2\pi \approx 0.29$ MHz, $\frac{\omega_0}{2} \approx 10.21$ MHz, $A \approx 1.25$ V, $B \approx 1.30$ V, and $\tau \approx 0.27$ μs, which are consistent with (*30*) and fitting parameters in Fig. 2D. Note that the time gap between repeat laser pulses is 10 μs, which allows the resonator and sample to return to equilibrium before the arrival of the next pulse. The red dots and the black line in Fig. 2D show the Fourier transform of the time domain signal during the second stage and its fit in Fig. 2C.

Beating the thermal noise limit by thermal noise estimation

As shown in schematic Fig. 1 (A and B), thermal noise can be distinguished from instrumental detection noise at steady states using Eqs. 2 and 3 and extended to dynamic signal range by Eqs. 4 and 5. For the PTIR measurements, the steady state and dynamic signal

Downloaded from https://www.science.org on March 15, 2023

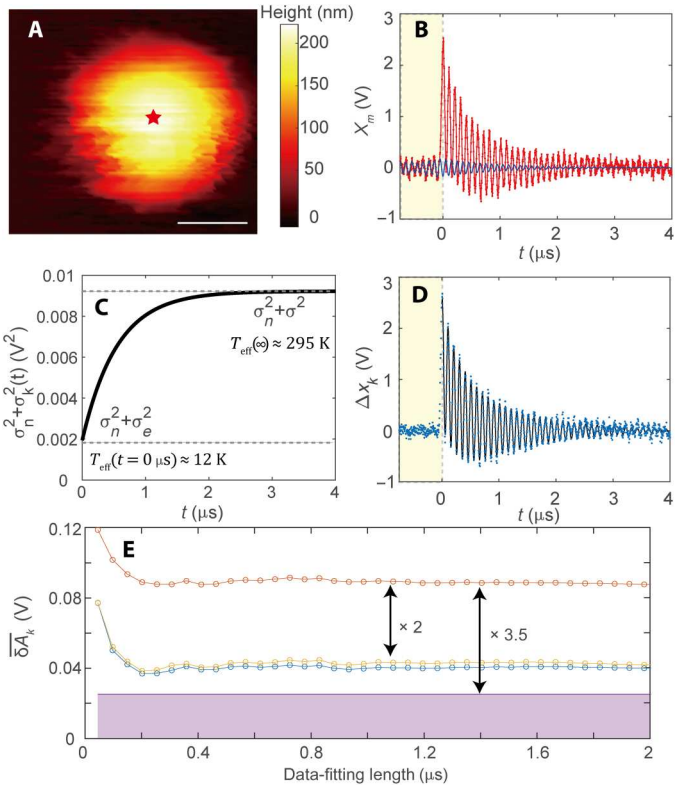

Fig. 4. Improving the precision of a PTIR measurement by removing thermal noise. (**A**) Topography of an SU-8 dome measured with a nanophotonic AFM probe. The star labels the detection point. Scale bar, 1 μm. (**B**) Measured excitation-ringdown signal triggered by laser pulse at $t = 0$ (red dots). The estimated thermal fluctuations are shown as blue dots. (**C**) Theoretical uncertainty of the data points at $t > 0$ given by Eq. 4. (**D**) PTIR signal after removal of the estimated thermal fluctuations is shown as blue dots. Its variance-weighted fit based on (C) and Eq. 1 is plotted as the black line. (**E**) SD of the fitting parameter A in Eq. 1 as a function of the after-pulse data-fitting length. The SD from fitting data before thermal noise subtraction (orange) and after thermal noise subtraction with equal (yellow) and inverse-variance (blue) weights is shown. The theoretical lower limit of the uncertainty of A due to detection noise and thermal fluctuations only is shown as the upper bound of the purple area. The experimentally obtained ≈2× precision improvement compared to the theoretical limit of ≈3.5× with the difference attributed to the effects of laser pulse timing jitter is shown.

time ranges correspond to the time intervals before and after the laser pulse, respectively. To validate this method, we first apply it to the purely steady-state case where the laser pulse is off. The blue dots in Fig. 3A shows the measured thermal fluctuations with detection uncertainty of the probe in contact with the sample. The detection noise is measured to be $\sigma_n^2 \approx 1.64 \times 10^{-3}$ V^2 under detection bandwidth BW ≈ 125 MHz, and thermal noise is $\sigma^2 \approx 7.58 \times 10^{-3}$ V^2. By definition, we obtain $\sigma_e^2 \approx 0.30 \times 10^{-3}$ V^2 and $\sigma_{dt}^2 \approx 5.52 \times 10^{-5}$ V^2 ($\sigma_n^2 + \sigma_e^2 \approx 1.94 \times 10^{-3}$ V^2, $\sigma_n^2 + \sigma^2 \approx 9.22 \times 10^{-3}$ V^2), corresponding to a cooling factor of $T/T_{\text{eff}} = \sigma^2/\sigma_e^2 \approx 25.3$, where T and T_{eff} are the effective equilibrium temperatures before and after the thermal subtraction, respectively. Although the measurement was conducted entirely at room temperature (T = 293 K), the maximum possible benefit of this noise subtraction strategy is equivalent to cooling the probe to ≈11.6 K immediately before the pulse. With these parameters, we estimate thermal fluctuations $\hat{u}_k$ in the rotating frame (ωiω$_0$) and then convert it back to the experimental frame as $\hat{x}_k = \frac{1}{2}(\hat{u}_k e^{i\omega t} + \hat{u}_k{}^* e^{-i\omega t})$. The sequential estimation is updated by each measured data point using Eqs. 2 and 3 up to t = 4 μs (Fig. 3A, yellow area), mimicking the starting of the pulse (transient state). The estimation at $t > 4$ μs (white area) is only based on the correlation of prior measurement at $t < 4$ μs without using any new data points as Eq. 5. The estimated thermal fluctuations $\hat{X}_k = \{\hat{x}_1, \ldots \hat{x}_k\}$ shown as red dots are in good agreement with measured blue data points $X_{m,k} = \{x_{m,1}, \ldots x_{m,k}\}$. Figure 3B displays the residuals $\Delta\hat{x}_k = \hat{x}_k - x_m$ and their SD (red dashed lines).

To illustrate the improvement of measurement precision (cooling effect) after subtracting the thermal noise, we repeatedly apply this process on N = 1000 groups of separate data measured under the same conditions at the steady state and calculate the residual of the ith group of data as $\Delta\hat{X}_{i,k} = \{\Delta\hat{x}_{m,1}, \ldots \Delta\hat{x}_{m,k}\}$. Their SD at each data point is calculated as $D_k = \sqrt{\frac{1}{N}\sum_{i=1}^{N} \Delta\hat{X}_{i,k}{}^2}$ shown as the black line in Fig. 3C. The red dashed line shows the theoretical precision given by $\sqrt{\sigma_n^2 + \sigma_k^2(t)}$ based on Eqs. 2 and 4 at before and after t = 4 μs, respectively. Like the schematic in Fig. 1D, however, here, we include the measurement noise component. After t = 4 μs, the precision decreases from the converged steady-state value $\sqrt{\sigma_n^2 + \sigma_e^2}$ to its original value $\sqrt{\sigma_n^2 + \sigma^2}$ asymptotically within 2/Γ. Analogously, the effective temperature of the sensor increases asymptotically within 2/Γ. The blue line in Fig. 3C shows the SD of the data $X_{m,k}$ before subtracting the thermal noise. The good agreement between theory and measurement validates the method. It also experimentally demonstrates that this method largely improves the detection precision within the time frame where the transient response signal is strong (Fig. 2C within 2/Γ). These estimates have well-defined uncertainty, which is critical for fitting dynamic signals as shown later. Figure 3D shows the noise power spectral density of the original data $X_{m,k}$ and residual $\Delta\hat{X}_k$ before t = 4 μs as blue and black dots, respectively. It shows that the method removes the thermal noise well. The deviation from the detection noise background (gray dots) at low frequencies derives from the slow distance drift between the probe and the sample.

Next, we apply this method to the dynamic signal in PTIR measurements. The test sample is a SU-8 dome with topography shown in Fig. 4A. The signal measured at the center of the sample is shown in Fig. 4B. Following the routine described above, we estimate the thermal fluctuation state before the pulse (steady state) using Eq. 2 and 3 and after the pulse (dynamic signal) using Eq. 5. The estimated results are shown as the blue dots in Fig. 4B. Next, we subtracted the estimated thermal noise from the data and obtain the blue dots in Fig. 4D, hereafter processed data. The thermal noise is largely reduced before $t < 2/\Gamma \approx 1.1$ μs and easily seen for $t < 0$ μs compared to Fig. 4B. The processed data contain dynamic signal S (Eq. 1) on top of a combination of detection noise and residual thermal noise whose uncertainty is well defined by Eq. 4 as shown in Fig. 4C. Notably, the effective cooling of the sensor is close to maximum (T_{eff} = 12 K) at the time (≈100 ns) when the maximum peak to peak of the ringdown signal used for chemical imaging occurs (*27*, *28*).

Downloaded from https://www.science.org on March 15, 2023

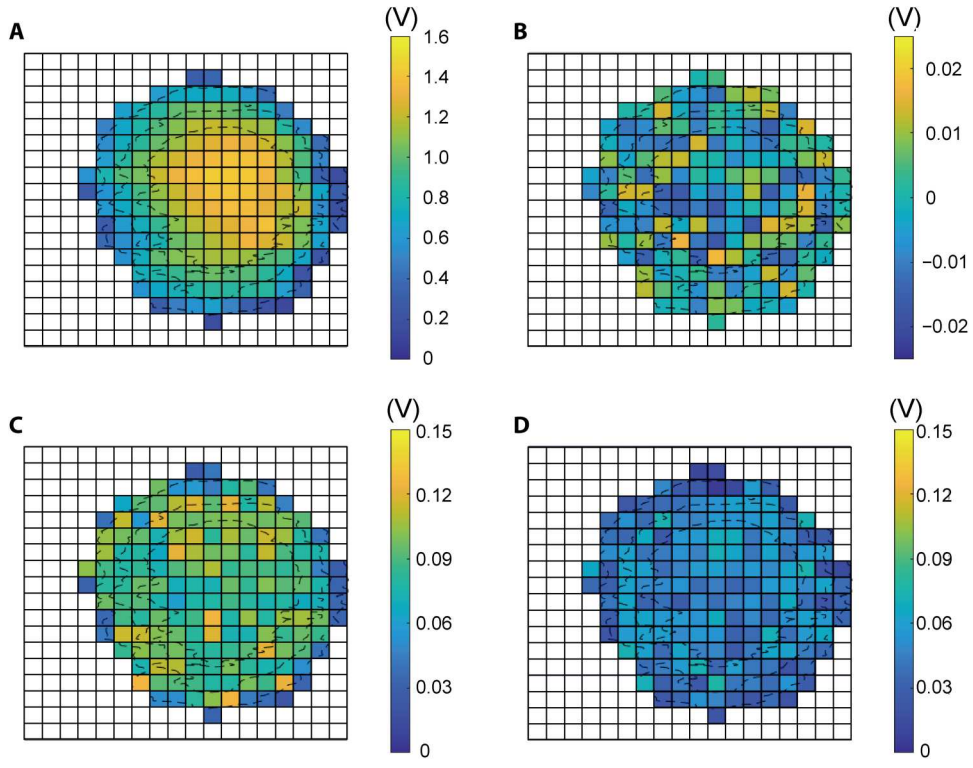

Fig. 5. Measured maps of the SU-8 dome. (**A**) Distribution of *A* on the SU-8 dome after removing thermal noise. The three dashed lines delimit the SU-8 heights of 20, 100, and 180 nm, respectively. (**B**) Difference between fitted *A* before and after removing the thermal noise, averaged from $N = 43$ datasets. (**C** and **D**) Distribution of uncertainty $\delta\overline{A_k}$ before and after removing thermal fluctuations. One SD uncertainty $\delta\overline{A_k}$ is calculated form $N = 43$ independent datasets. The pixel size is 140 nm by 140 nm.

To extract useful information from the PTIR measurement, such as oscillation amplitude *A* for spectroscopy (*35*) or sample's thermal constant τ for thermal conductivity analysis (*30*), a fitting process is necessary. The easiest option is to directly apply a least-square fit (LSF) to the processed data using Eq. 1. The reduced thermal noise (effective temperature) lowers the uncertainty of the fit. In addition, the processed data at each point have a known and different uncertainty or variance, i.e., heteroscedasticity, as shown in Fig. 4C. The standard procedure for fitting data with heteroscedasticity is weighted LSF (WLSF) (*41*) where the weight is defined as the inverse of the variance of each point, $W_{kk} = \frac{1}{D_k^2}$. In WLSF, the strong signals at the beginning also have less uncertainty and more weight. It makes the WLSF further improve the precision of fitting results. The time complexity of WLSF is the same as the LSF, meaning that it does not reduce the throughputs of the measurement. It is critical since one of the important impacts of the thermal noise subtraction method is improving the throughput. The WLSF result of the data using Eq. 1 is shown as the black line in Fig. 4D.

One fitting parameter that we aim to measure in PTIR is the amplitude *A*, which is proportional to the absorption coefficient (*40*, *42*), thus enabling IR spectroscopy at the nanoscale. To demonstrate the improvement in the fitting precision, we apply this method on $N = 1000$ groups of repeating excitation-ringdown data similar to Fig. 4B, with nominally the same pulse power and location on the sample. $A_{i,k}$ denotes the fitted *A* from the first *k* points after $t > 0$ of the *i*th data group. Figure 4E shows the SD of $A_{i,k}$, $\delta\overline{A_k} = \sqrt{\frac{1}{N}\sum_{i=1}^{N}\left(A_{i,k} - \frac{1}{N}\sum_{i=1}^{N}A_{i,k}\right)^2}$, for data without thermal noise subtraction (orange), with thermal noise subtraction using LSF (yellow), and with thermal noise subtraction using WLSF (blue).

We make the following observations. First, the fit converges quickly at $t \approx 0.2$ μs, i.e., fitting to the signal within 0 μs < *t* < 0.2 μs provides comparable precision to fitting to a longer 0 μs < *t* < 2 μs trace. Second, the improvement from thermal noise subtraction is around 2×, doubling the measurement sensitivity for the same averaging time or, equivalently, doubling its throughput. Meanwhile, the improvement from using WLSF versus LSF is limited. Different choice of weights for the remaining data point makes a small difference in our measurement. However, we point out that if the detection noise is strong such that the converging time is longer, their difference will be larger. Last, we provide a theoretical precision limit for the estimate of *A* in our setup (upper bound of the purple area) based on an optimal Bayesian estimator (*17*) for a stepwise excitation (see Materials and Methods). Theoretically, the improvement can reach around 3.5× for the specific level of the detection noise in our experiment and continues to improve with decreasing detection noise. This thermal noise avoidance technique is practically limited only by the instrumentation factors. The difference between experimentally demonstrated precision and the theory can be attributed to the nonoptimal WLSF and other noise

Downloaded from https://www.science.org on March 15, 2023

sources, such as the timing jitter of the pulsed laser, which affects the start $t = 0$.

Using this method, we scan the probe on the SU-8 sample and fit the cantilever oscillation amplitude A (i.e., the PTIR signal used in practice) at each location (see Fig. 5A). The distribution of A agrees well with the height distribution (Fig. 4A) since the absorbed light intensity and the resulting thermal expansion are proportional to the thickness of the thin sample (*40*, *42*). The dashed lines show the thickness contours of 20, 100, and 180 nm from the periphery toward the inside. The measurements on the bare substrate surrounding the sample (without PTIR signal) are excluded and shown as white. We also compare the fitted A before and after removing thermal fluctuations; their difference is shown in Fig. 5B. The subtle differences evenly distributed on the map have a nearly zero-mean value (mean value of Fig. 5B ≈0.0012 is significantly smaller than its SD≈0.0087), meaning the method is not strongly biased, consistent with numerical simulation on a similar model (damped harmonic oscillator) (*43*). In contrast, the precision of A obtained using thermal noise removal shown in Fig. 5D is strongly improved relative to that in Fig. 5C. The precision is doubled by applying this method, i.e., the averaged uncertainty $\delta\overline{A_k} \approx 0.095$ shown in Fig. 5C is nearly twice the $\delta\overline{A_k} \approx 0.049$ in Fig. 5D.

DISCUSSION

We developed a method for thermal noise avoidance in measurements of dynamic signals obtained with resonant transducers by optimally estimating and subtracting thermal fluctuations in the presence of instrumental detection noise. Using an experimental setup that uses a cavity optomechanical AFM probe as its displacement transducer, we obtain a 25× reduction of the transducer's effective temperature consistent with the theory. The accurate steady-state estimation of the probe state is extrapolated forward in time and subtracted from the subsequently induced dynamically varying transient signal of interest, reducing its measurement uncertainty by 2× approaching the theoretical limit of ≈3.5× under our experimental conditions.

By removing thermal noise from transient dynamic signals, we experimentally improve the sensing precision and throughput of our measurements. Beyond the field of nanomechanical sensing, the method presented here is broadly applicable to other optical, acoustic, and radiofrequency resonant transducers for which the measurements are limited by thermal noise. This work advances the general understanding and management of thermal noise. It provides an easy-to-apply and general method that improves precision, sensitivity, and throughput for thermal noise–limited dynamic signals.

MATERIALS AND METHODS

Extend the estimation of steady-state signal to dynamic signal

To extrapolate the estimation from steady-state signal into the time range of the dynamic response, we need to update Eqs. 2 and 3 without using new data points. Equations 2 and 3 change to

$$\sigma_k^2 = \sigma_{k-1}^2 e^{-\Gamma dt} + \sigma_{dt}^2 \tag{MM1}$$

$$\hat{u}_k = \hat{u}_{k-1} e^{\left(i\Delta\omega - \frac{\Gamma}{2}\right)dt} \tag{MM2}$$

We rewrite Eq. MM1 in continuous form. By setting $\sigma_{k-1}^2 = y$, we have

$$y + dy = ye^{-\Gamma dt} + \Gamma dt\sigma^2 \tag{MM3}$$

After doing integration with the initial condition of $y(0) = \sigma_e^2 = \frac{\sqrt{\eta^2+4}-\eta}{2}\eta\sigma^2$, where σ_e^2 is the converged uncertainty at the steady states (*17*) and $\eta = \sqrt{\frac{\sigma_n^2 \Gamma dt}{\sigma^2}}$, we get

$$\sigma_k^2(t) = \sigma^2 + [\sigma_k^2(0) - \sigma^2]e^{-\Gamma t} \tag{MM4}$$

$\sigma_k^2(t)$ increase from $\sigma_e^2 = \frac{\sqrt{\eta^2+4}-\eta}{2}\eta\sigma^2$ at $t = 0$ to σ^2 at $t >> 1/\Gamma$, equivalent to the effective temperature increases from $T_{\text{eff}} = T\frac{\sigma_e^2}{\sigma^2}$ (where $\sigma_e^2 \ll \sigma^2$ for thermal noise–limited sensors) back to the environmental temperature T.

Similarly, Eq. 3 can also be written in the continuous form

$$\hat{u}_k(t) = \hat{u}_k(0) e^{\left(i\Delta\omega - \frac{\Gamma}{2}\right)t} \tag{MM5}$$

where $\hat{u}_k(0)$ is the last estimated position at the steady states.

Optimal Bayesian estimator for a stepwise excitation

In the PTIR measurement, the parameters of interest are B and A in Eq. 1, i.e., the stepwise function amplitude (sample's instantaneous expansion) and the resulting response of the sensor (probe's oscillating amplitude), respectively. If the probe can be regarded as a mass point, $A = B$. In our case, $A = cB$, where the proportionality constant c depends on the geometry of the probe and the contact point on the probe. On the basis of the finite-element simulation, $c \approx 1.0$ for our probe (*44*).

To estimate the stepwise function's amplitude B, we first assume that the step occurs at $t = 0$. We perform the "forward" Bayesian estimation at the steady states from $t = -\infty$ to 0^- using Eqs. 2 and 3, and get the estimated position $\hat{u}(0^-)$ at $t = 0^-$ before the pulse with the converged uncertainty of $\sigma_e^2 = \frac{\sqrt{\eta^2+4}-\eta}{2}\eta\sigma^2$ (*17*). Similarly, we perform a "backward estimation" of the position immediately after the pulse $\hat{u}(0^+)$ based on data from $t = +\infty$ to 0^+ using the time-reversal function of Eqs. 2 and 3 as

$$\frac{1}{\sigma_k^2} = \frac{1}{\sigma_{k-1}^2 e^{+\Gamma dt} + \sigma_{dt}^2} + \frac{1}{\sigma_n^2} \tag{MM6}$$

$$\hat{u}_k = \left[\frac{1}{\sigma_{k-1}^2 e^{+\Gamma dt} + \sigma_{dt}^2} e^{-\left(i\Delta\omega - \frac{\Gamma}{2}\right)dt}\hat{u}_{k-1} + \frac{1}{\sigma_n^2}u_{m,k}\right] \times \left(\frac{1}{\sigma_{k-1}^2 e^{+\Gamma dt} + \sigma_{dt}^2} + \frac{1}{\sigma_n^2}\right)^{-1} \tag{MM7}$$

We get the estimated position $\hat{u}(0^+)$ at $t = 0^+$ after the pulse with the converged uncertainty of $\sigma_{e+}^2 = \frac{\sqrt{\eta^2+4}+4}{2}\eta\sigma^2$.

Downloaded from https://www.science.org on March 15, 2023

By definition, $B = \hat{u}(0^+) - \hat{u}(0^-)$. If its uncertainty is solely from the thermal noise and detection noise, after subtraction, the one SD uncertainty can be expressed as $\sqrt{\sigma_{e+}^2 + \sigma_e^2}$. The purple line in Fig. 4 is calculated from $\sqrt{\sigma_{e+}^2 + \sigma_e^2}$ as if only thermal noise and detection noise are present in our measurement.

Commercial products disclaimer

The full description of the procedures used in this paper requires the identification of certain commercial products. The inclusion of this information should in no way be construed as indicating that these products are endorsed by the National Institute of Standards and Technology (NIST) or are recommended by NIST or that they are necessarily the best materials for the purposes described.

REFERENCES AND NOTES

1. J. Moser, J. Güttinger, A. Eichler, M. J. Esplandiu, D. E. Liu, M. I. Dykman, A. Bachtold, Ultrasensitive force detection with a nanotube mechanical resonator. *Nat. Nanotechnol.* **8**, 493–496 (2013).
2. D. Rugar, R. Budakian, H. J. Mamin, B. W. Chui, Single spin detection by magnetic resonance force microscopy. *Nature* **430**, 329–332 (2004).
3. A. K. Naik, M. S. Hanay, W. K. Hiebert, X. L. Feng, M. L. Roukes, Towards single-molecule nanomechanical mass spectrometry. *Nat. Nanotechnol.* **4**, 445–450 (2009).
4. J. Chaste, A. Eichler, J. Moser, G. Ceballos, R. Rurali, A. Bachtold, A nanomechanical mass sensor with yoctogram resolution. *Nat. Nanotechnol.* **7**, 301–304 (2012).
5. J. E. Losby, F. F. Sani, D. T. Grandmont, Z. Diao, M. Belov, J. A. J. Burgess, S. R. Compton, W. K. Hiebert, D. Vick, K. Mohammad, E. Salimi, G. E. Bridges, D. J. Thomson, M. R. Freeman, Torque-mixing magnetic resonance spectroscopy. *Science* **350**, 798–801 (2015).
6. A. N. Cleland, M. L. Roukes, A nanometre-scale mechanical electrometer. *Nature* **392**, 160–162 (1998).
7. V. T. K. Sauer, Z. Diao, J. N. Westwood-Bachman, M. R. Freeman, W. K. Hiebert, Single laser modulated drive and detection of a nano-optomechanical cantilever. *AIP Adv.* **7**, 015115 (2017).
8. E. Sage, A. Brenac, T. Alava, R. Morel, C. Dupré, M. S. Hanay, M. L. Roukes, L. Duraffourg, C. Masselon, S. Hentz, Neutral particle mass spectrometry with nanomechanical systems. *Nat. Commun.* **6**, 1–5 (2015).
9. A. W. Barnard, M. Zhang, G. S. Wiederhecker, M. Lipson, P. L. McEuen, Real-time vibrations of a carbon nanotube. *Nature* **566**, 89–93 (2019).
10. E. E. Wollman, C. U. Lei, A. J. Weinstein, J. Suh, A. Kronwald, F. Marquardt, A. A. Clerk, K. C. Schwab, Quantum squeezing of motion in a mechanical resonator. *Science* **349**, 952–955 (2015).
11. P. R. Saulson, Thermal noise in mechanical experiments. *Phys. Rev. D* **42**, 2437–2445 (1990).
12. M. Wang, D. J. Perez-Morelo, V. Aksyuk, Overcoming thermo-optical dynamics in broadband nanophotonic sensing. *Microsyst. Nanoeng.* **7**, 52 (2021).
13. M. Wang, R. Zhang, R. Ilic, V. Aksyuk, Y. Liu, Frequency stabilization of nanomechanical resonators using thermally invariant strain engineering. *Nano Lett.* **20**, 3050–3057 (2020).
14. D. Guan, Z. H. Hang, Z. Marcet, H. Liu, I. I. Kravchenko, C. T. Chan, H. B. Chan, P. Tong, Direct measurement of optical force induced by near-field plasmonic cavity using dynamic mode AFM. *Sci. Rep.* **5**, 16216 (2015).
15. I. M. Malovichko, Measuring AFM cantilever stiffness from a thermal noise spectrum. *Bull. Russ. Acad. Sci. Phys.* **77**, 972–974 (2013).
16. R. Leijssen, G. R. La Gala, L. Freisem, J. T. Muhonen, E. Verhagen, Nonlinear cavity optomechanics with nanomechanical thermal fluctuations. *Nat. Commun.* **8**, ncomms16024 (2017).
17. M. Wang, R. Zhang, R. Ilic, Y. Liu, V. A. Aksyuk, Fundamental limits and optimal estimation of the resonance frequency of a linear harmonic oscillator. *Commun. Phys.* **4**, 207 (2021).
18. C. Ma, C. Zhou, J. Peng, Y. Chen, W. Arnold, J. Chu, Thermal noise in contact atomic force microscopy. *J. Appl. Phys.* **129**, 234303 (2021).
19. F. Gittes, C. F. Schmidt, Thermal noise limitations on micromechanical experiments. *Eur. Biophys. J.* **27**, 75–81 (1998).
20. K. V. Poletkin, J. G. Korvink, V. Badilita, V. Mechanical, Mechanical thermal noise in micromachined levitated two-axis rate gyroscopes. *IEEE Sensors J.* **18**, 1390–1402 (2018).
21. F. Mohd-Yasin, D. J. Nagel, C. E. Korman, Noise in MEMS. *Meas. Sci. Technol.* **21**, 012001 (2010).
22. R. P. Leland, Mechanical-thermal noise in MEMS gyroscopes. *IEEE Sensors J.* **5**, 493–500 (2005).
23. A. H. Ghadimi, S. A. Fedorov, N. J. Engelsen, M. J. Bereyhi, R. Schilling, D. J. Wilson, T. J. Kippenberg, Elastic strain engineering for ultralow mechanical dissipation. *Science* **360**, 764–768 (2018).
24. J. D. Teufel, T. Donner, D. Li, J. W. Harlow, M. S. Allman, K. Cicak, A. J. Sirois, J. D. Whittaker, K. W. Lehnert, R. W. Simmonds, Sideband cooling of micromechanical motion to the quantum ground state. *Nature* **475**, 359–363 (2011).
25. H. M. Wiseman, Quantum theory of continuous feedback. *Phys. Rev. A* **49**, 2133–2150 (1994).
26. A. Centrone, Infrared imaging and spectroscopy beyond the diffraction limit. *Annu. Rev. Anal. Chem.* **8**, 101–126 (2015).
27. D. Kurouski, A. Dazzi, R. Zenobi, A. Centrone, Infrared and Raman chemical imaging and spectroscopy at the nanoscale. *Chem. Soc. Rev.* **49**, 3315–3347 (2020).
28. J. J. Schwartz, D. S. Jakob, A. A. Centrone, A guide to nanoscale IR spectroscopy: Resonance enhanced transduction in contact and tapping mode AFM-IR. *Chem. Soc. Rev.* **51**, 5248–5267 (2022).
29. J. Chae, S. An, G. Ramer, V. Stavila, G. Holland, Y. Yoon, A. A. Talin, M. Allendorf, V. A. Aksyuk, A. Centrone, Nanophotonic atomic force microscope transducers enable chemical composition and thermal conductivity measurements at the nanoscale. *Nano Lett.* **17**, 5587–5594 (2017).
30. M. Wang, G. Ramer, D. J. Perez-Morelo, G. Pavlidis, J. J. Schwartz, L. Yu, R. Ilic, V. A. Aksyuk, A. Centrone, High throughput nanoimaging of thermal conductivity and interfacial thermal conductance. *Nano Lett.* **22**, 4325–4332 (2022).
31. A. M. Katzenmeyer, G. Holland, K. Kjoller, A. Centrone, Absorption spectroscopy and imaging from the visible through mid-infrared with 20 nm resolution. *Anal. Chem.* **87**, 3154–3159 (2015).
32. A. M. Katzenmeyer, J. Canivet, G. Holland, D. Farrusseng, A. Centrone, Assessing chemical heterogeneity at the nanoscale in mixed-ligand metal-organic frameworks with the PTIR technique. *Angew. Chem. Int. Ed.* **53**, 2852–2856 (2014).
33. J. J. Schwartz, H. J. Chuang, M. R. Rosenberger, S. V. Sivaram, K. M. McCreary, B. T. Jonker, A. Centrone, Chemical identification of interlayer contaminants within van der Waals heterostructures. *ACS Appl. Mater. Interfaces* **11**, 25578–25585 (2019).
34. X. Ma, G. Pavlidis, E. Dillon, V. Beltran, J. J. Schwartz, M. Thoury, F. Borondics, C. Sandt, K. Kjoller, B. H. Berrie, A. Centrone, Micro to nano: Multiscale IR analyses reveal zinc soap heterogeneity in a 19th-century painting by corot. *Anal. Chem.* **94**, 3103–3110 (2022).
35. F. S. Ruggeri, B. Mannini, R. Schmid, M. Vendruscolo, T. P. J. Knowles, Single molecule secondary structure determination of proteins through infrared absorption nanospectroscopy. *Nat. Commun.* **11**, 2945 (2020).
36. J. Chae, Q. Dong, J. Huang, A. Centrone, Chloride incorporation process in $CH_3NH_3PbI_{3-x}Cl_x$ perovskites via nanoscale bandgap maps. *Nano Lett.* **15**, 8114–8121 (2015).
37. A. M. Katzenmeyer, J. Chae, R. Kasica, G. Holland, B. Lahiri, A. Centrone, Nanoscale imaging and spectroscopy of plasmonic modes with the PTIR technique. *Adv. Opt. Mater.* **2**, 718–722 (2014).
38. J. J. Schwartz, S. T. le, S. Krylyuk, C. A. Richter, A. V. Davydov, A. Centrone, Substrate-mediated hyperbolic phonon polaritons in MoO_3. *Nanophotonics* **10**, 1517–1527 (2021).
39. J. J. Schwartz, G. Pavlidis, A. Centrone, Understanding cantilever transduction efficiency and spatial resolution in nanoscale infrared microscopy. *Anal. Chem.* **94**, 13126–13135 (2022).
40. G. Ramer, V. A. Aksyuk, A. Centrone, Quantitative chemical analysis at the nanoscale using the photothermal induced resonance technique. *Anal. Chem.* **89**, 13524–13531 (2017).
41. W. H. Press, S. A. Eukolsky, W. T. Vetterling, B. P. Flannery, *Numerical Recipes: The Art of Scientific Computing* (Cambridge Univ. Press, ed. 3, 2007).
42. B. Lahiri, G. Holland, A. Centrone, Chemical imaging beyond the diffraction limit: Experimental validation of the PTIR technique. *Small* **9**, 439–445 (2013).
43. K. Fogelmark, M. A. Lomholt, A. Irbäck, T. Ambjörnsson, Fitting a function to time-dependent ensemble averaged data. *Sci. Rep.* **8**, 6984 (2018).
44. S. M. An, J. Zou, G. Holland, J. Chae, A. Centrone, V. Aksyuk, Optomechanical transducer-based soft and high frequency nanoscale cantilever for atomic force microscopy, in *Proceedings of the Solid State Sensor, Actuator and Microsystems Workshop*, Hilton Head Island, SC, USA, 5 to 9 June 2016 (2016).

Acknowledgments: We thank Y. Yan, X. Lu, and J. A. Liddle for reviewing this paper and giving meaningful suggestions. **Funding:** M.W., D.J.P.-M., and J.J.S. were supported under the Corporative Research Agreement Award 70NANB10H193, through the University of Maryland. Research was performed in part at the NIST Center for Nanoscale Science and Technology.
Author contributions: Metrology and data analysis: M.W. Setup optimization: M.W., D.J.P.-M., G.R., J.J.S., and G.P. Probe fabrication: D.J.P.-M. and M.W. Sample preparation: L.Y. and R.I. Supervision: V.A.A. and A.C. Writing—original draft: M.W. and V.A.A. Writing—review and

Downloaded from https://www.science.org on March 15, 2023

editing: M.W., D.J.P.-M., G.R., J.J.S., G.P., A.C., and V.A.A. **Competing interests:** The authors declare that they have no competing interests. **Data and materials availability:** All data needed to evaluate the conclusions in the paper are present in the paper and available at the NIST Public Data Repository (doi: 10.18434/mds2-2926).

Submitted 14 November 2022
Accepted 13 February 2023
Published 15 March 2023
10.1126/sciadv.adf7595

Downloaded from https://www.science.org on March 15, 2023

ScienceAdvances

Beating thermal noise in a dynamic signal measurement by a nanofabricated cavity optomechanical sensor

Mingkang Wang, Diego J. Perez-Morelo, Georg Ramer, Georges Pavlidis, Jeffrey J. Schwartz, Liya Yu, Robert Ilic, Andrea Centrone, and Vladimir A. Aksyuk

Sci. Adv., **9** (11), eadf7595.
DOI: 10.1126/sciadv.adf7595

View the article online
https://www.science.org/doi/10.1126/sciadv.adf7595
Permissions
https://www.science.org/help/reprints-and-permissions

Downloaded from https://www.science.org on March 15, 2023

Use of this article is subject to the Terms of service

Science Advances (ISSN) is published by the American Association for the Advancement of Science. 1200 New York Avenue NW, Washington, DC 20005. The title *Science Advances* is a registered trademark of AAAS.
Copyright © 2023 The Authors, some rights reserved; exclusive licensee American Association for the Advancement of Science. No claim to original U.S. Government Works. Distributed under a Creative Commons Attribution NonCommercial License 4.0 (CC BY-NC).